OBSERVATION OF ANISOTROPY
OF TEV COSMIC RAYS WITH TWO YEARS OF HAWC

A.U. Abeysekara,[1] R. Alfaro,[2] C. Alvarez,[3] R. Arceo,[3] J.C. Arteaga-Velázquez,[4]
D. Avila Rojas,[2] H.A. Ayala Solares,[5] A. Becerril,[2] E. Belmont-Moreno,[2] S.Y. BenZvi,[6]
A. Bernal,[7] J. Braun,[8] K.S. Caballero-Mora,[3] T. Capistrán,[9] A. Carramiñana,[9]
S. Casanova,[10, 11] M. Castillo,[4] U. Cotti,[4] J. Cotzomi,[12] C. De León,[12] E. De la Fuente,[13]
R. Diaz Hernandez,[9] S. Dichiara,[7] B.L. Dingus,[14] M.A. DuVernois,[8] J.C. Díaz-Vélez,[13]
K. Engel,[15] D.W. Fiorino,[15] N. Fraija,[7] J.A. García-González,[2] F. Garfias,[7]
A. González Muñoz,[2] M.M. González,[7] J.A. Goodman,[15] Z. Hampel-Arias,[8, 16]
J.P. Harding,[14] S. Hernandez,[2] B. Hona,[17] F. Hueyotl-Zahuantitla,[3] C.M. Hui,[18]
P. Hüntemeyer,[17] A. Iriarte,[7] A. Jardin-Blicq,[11] V. Joshi,[11] S. Kaufmann,[3] A. Lara,[19]
R.J. Lauer,[20] W.H. Lee,[7] H. León Vargas,[2] A.L. Longinotti,[9] G. Luis-Raya,[21]
R. Luna-García,[22] D. López-Cámara,[23, 23] R. López-Coto,[24, 11] D. López-Cámara,[23, 23]
R. López-Coto,[24, 11] K. Malone,[5] S.S. Marinelli,[25] O. Martinez,[12]
I. Martinez-Castellanos,[15] J. Martínez-Castro,[22] H. Martínez-Huerta,[26] J.A. Matthews,[20]
P. Miranda-Romagnoli,[27] E. Moreno,[12] M. Mostafá,[5] A. Nayerhoda,[10] L. Nellen,[28]
M. Newbold,[1] M.U. Nisa,[6] R. Noriega-Papaqui,[27] R. Pelayo,[22] J. Pretz,[5]
E.G. Pérez-Pérez,[21] Z. Ren,[20] C.D. Rho,[6] C. Rivière,[15] D. Rosa-González,[9] M. Rosenberg,[5]
E. Ruiz-Velasco,[11] F. Salesa Greus,[10] A. Sandoval,[2] M. Schneider,[29] H. Schoorlemmer,[11]
M. Seglar Arroyo,[5] G. Sinnis,[14] A.J. Smith,[15] R.W. Springer,[1] P. Surajbali,[11] I. Taboada,[30]
O. Tibolla,[3] K. Tollefson,[25] I. Torres,[9] G. Vianello,[31] L. Villaseñor,[12] T. Weisgarber,[8]
F. Werner,[11] S. Westerhoff,[8] J. Wood,[8] T. Yapici,[6] et al.

[1] *Department of Physics and Astronomy, University of Utah, Salt Lake City, UT, USA*
[2] *Instituto de Física, Universidad Nacional Autónoma de México, Mexico City, Mexico*
[3] *Universidad Autónoma de Chiapas, Tuxtla Gutiérrez, Chiapas, Mexico*
[4] *Universidad Michoacana de San Nicolás de Hidalgo, Morelia, Mexico*
[5] *Department of Physics, Pennsylvania State University, University Park, PA, USA*
[6] *Department of Physics & Astronomy, University of Rochester, Rochester, NY, USA*
[7] *Instituto de Astronomía, Universidad Nacional Autónoma de México, Mexico City, Mexico*
[8] *Department of Physics, University of Wisconsin-Madison, Madison, WI, USA*
[9] *Instituto Nacional de Astrofísica, ptica y Electrónica, Tonantzintla, Puebla, Mexico*
[10] *Institute of Nuclear Physics Polish Academy of Sciences, PL-31342 IFJ-PAN, Krakow, Poland*
[11] *Max-Planck Institute for Nuclear Physics, Heidelberg, Germany*
[12] *Facultad de Ciencias Físico Matemáticas, Benemérita Universidad Autónoma de Puebla, Puebla, Mexico*
[13] *Departamento de Física, Centro Universitario de Ciencias Exactase Ingenierias, Universidad de Guadalajara, Guadalajara, Mexico*
[14] *Physics Division, Los Alamos National Laboratory, Los Alamos, NM, USA*
[15] *Department of Physics, University of Maryland, College Park, MD, USA*
[16] *Inter-university Institute for High Energies, Université Libre de Bruxelles, Bruxelles, Belgium*
[17] *Department of Physics, Michigan Technological University, Houghton, MI, USA*
[18] *NASA Marshall Space Flight Center, Astrophysics Office, Huntsville, AL, USA*
[19] *Instituto de Geofísica, Universidad Nacional Autónoma de México, Mexico City, Mexico*
[20] *Department of Physics and Astronomy, University of New Mexico, Albuquerque, NM, USA*

2

[21] *Universidad Politecnica de Pachuca, Pachuca, Hidalgo, Mexico*
[22] *Centro de Investigación en Computación, Instituto Politécnico Nacional, Mexico City, Mexico*
[23] *Cátedras Conacyt—Instituto de Astronomía, Universidad Nacional Autónoma de México, Mexico City, Mexico*
[24] *INFN and Universita di Padova, via Marzolo 8, I-35131,Padova,Italy*
[25] *Department of Physics and Astronomy, Michigan State University, East Lansing, MI, USA*
[26] *Physics Department, Centro de Investigacion y de Estudios Avanzados del IPN, Mexico City, Mexico*
[27] *Universidad Autónoma del Estado de Hidalgo, Pachuca, Mexico*
[28] *Instituto de Ciencias Nucleares, Universidad Nacional Autónoma de México, Mexico City, Mexico*
[29] *Santa Cruz Institute for Particle Physics, University of California, Santa Cruz, Santa Cruz, CA, USA*
[30] *School of Physics and Center for Relativistic Astrophysics - Georgia Institute of Technology, Atlanta, GA, USA*
[31] *Department of Physics, Stanford University, Stanford, CA, USA*

ABSTRACT

After two years of operation, the High-Altitude Water Cherenkov (HAWC) Observatory has analyzed the TeV cosmic-ray sky over an energy range between 2.0 and 72.8 TeV. Like other detectors in the northern and southern hemispheres, HAWC observes an energy-dependent anisotropy in the arrival direction distribution of cosmic rays. This anisotropy is dominated by a dipole moment with phase in right ascension $\alpha \approx 40°$ and amplitude that slowly rises in relative intensity from 8×10^{-4} at 2 TeV to 14×10^{-4} around 30 TeV , above which the dipole decreases in strength. A significant large-scale ($> 60°$ in angular extent) signal is also observed in the quadrupole and octupole moments, and significant small-scale features are also present, with locations and shapes consistent with previous observations. Compared to previous measurements in this energy range, the HAWC cosmic-ray sky maps improve on the energy resolution and fit precision of the anisotropy. These data can be used in an effort to better constrain local cosmic-ray accelerators and the intervening magnetic fields.

Keywords: astroparticle physics — cosmic rays — large-scale anisotropy — dipole — magnetic fields

1. INTRODUCTION

The study of the anisotropy in the arrival direction of cosmic rays has entered an era of precision measurement. Combined with improved modeling of the local interstellar medium, these measurements are maturing into an important way to understand simultaneously cosmic-ray acceleration and propagation. For a recent review see (Ahlers & Mertsch 2016).

Anisotropy is a well-studied consequence of standard propagation models where cosmic rays diffuse due to random magnetic fields and their sources are distributed inhomogeneously (Erlykin & Wolfendale 2006; Blasi & Amato 2012; Pohl & Eichler 2013; Sveshnikova et al. 2013). Anisotropy can also arise from motion relative to the rest frame of the cosmic rays (Compton & Getting 1935). Both scenarios result in a dominantly dipolar anisotropy, yet the predicted dipole amplitude is at least an order of magnitude larger than the observed value (Kumar & Eichler 2014; Mertsch & Funk 2015), and the measured dipole orientation can not be explained by these simple models. Recent studies have included the effects of regular magnetic fields to probe the origins of the dipole direction (Ahlers et al. 2016) in hopes of identifying the locations of accelerators contributing most to the locally observed cosmic-ray flux.

While the observed TeV cosmic-ray anisotropy is primarily dipolar with amplitude $\sim 10^{-3}$, it also contains smaller scale structure $O(\lesssim 45°)$ with strength $\sim 10^{-4}$. It is likely that an initial dipolar distribution is distorted as it passes through the interstellar medium. For example, isotropic magnetic turbulence can create a feed down of angular power to higher multipole moments (Giacinti & Sigl 2012; Ahlers 2014; Ahlers & Mertsch 2015; Giacinti & Kirk 2017), and pitch-angle scattering (Giacinti & Kirk 2017) alters the shape of the large-scale multipoles. It is possible that heliospheric effects perturb the anisotropy, manifesting in the observed small-scale structure (Desiati & Lazarian 2013; Schwadron et al. 2014). Anisotropy can also result from non-standard diffusion such as strong regularities in local magnetic field lines (Drury 2013; Harding et al. 2016). Thus, divergence from a pure dipole anisotropy provides a probe into the bulk properties of the interstellar medium.

Measuring anisotropy signals of $O(10^{-3} - 10^{-4})$ at significant levels requires several key detector attributes. A large instantaneous sky-coverage and long, uninterrupted observation periods are needed to achieve statistical uncertainties below the signal strength and to resolve features with large angular extent ($180°$). Only earthbound air-shower detectors fit these requirements, combining large fields-of-view, effective areas of $\sim 10^4$ m^2, and high duty cycles with long-term stability.

Cosmic-ray anisotropy has been observed in the energy range ~ 500 GeV - 100 PeV by air shower arrays such as Tibet-ASγ (Amenomori et al. 2005a, 2006, 2017), Milagro (Abdo et al. 2008, 2009), EAS-TOP (Aglietta et al. 2009), IceCube/IceTop (Abbasi et al. 2010, 2011, 2012; Aartsen et al. 2013, 2016), ARGO-YBJ (Di Sciascio 2013; Bartoli et al. 2013, 2015), and HAWC (Abeysekara et al. 2014). Below these energies, cosmic rays begin to follow geomagnetic field lines and no longer probe interstellar scales. Only the Pierre Auger Observatory has a significant measurement (Aab et al. 2017a,b) above EeV energies. The most recent experimental overviews are given in (Di Sciascio & Iuppa 2014) and in (Ahlers & Mertsch 2016).

Air shower arrays must use the observations themselves to determine intrinsic detector acceptances, which limits sensitivity to the anisotropy component along the direction of the Earth's rotation, i.e. along the right ascension α in equatorial coordinates. These detectors are thus unable to recover a dipolar signal aligned with the equatorial poles, bounding the maxi-

mally recoverable dipole strength according to its orientation in declination. Direct modeling of the detector acceptance, as done in (Aab et al. 2017a) can eliminate this bias but has not been demonstrated for arrays operating at TeV energies, as it requires an agreement between simulation and data over the full zenith angle range at the level of 10^{-5} or better, which is currently not achieved.

In this paper, we describe the results of an analysis of the cosmic-ray anisotropy on all angular scales and as a function of energy using the first two years of data recorded by the HAWC experiment. In a previous paper (Abeysekara et al. 2014), we used 113 days of data to study the small-scale anisotropy of cosmic rays above 1.7 TeV. Here, we extend on this analysis by also studying the large-scale anisotropy and using an improved energy estimator (Alfaro et al. 2017) to study the energy-dependence of both the small- and large-scale structures.

In addition, we apply a new iterative method (Ahlers et al. 2016) to reconstruct the maximally recoverable strength of the anisotropy. This method compensates for the reduction in the measured dipole strength caused by the fact that mid-latitude detectors only see a fraction of the cosmic-ray dipole at any given time.

With the first two years of data taking, the HAWC array can currently study the cosmic-ray anisotropy up to energies of about 70 TeV. In future studies, we will extend the energy range to higher energies, using the same methods described in this paper.

This paper is organized as follows: we first describe the HAWC detector in Section 2, then the event selection and data set used for the measurement in Section 3. An explanation of the analysis methods is provided in Section 4. The results of the observed anisotropy are presented and discussed in section 5. Section 6 summarizes the main conclusions of this work.
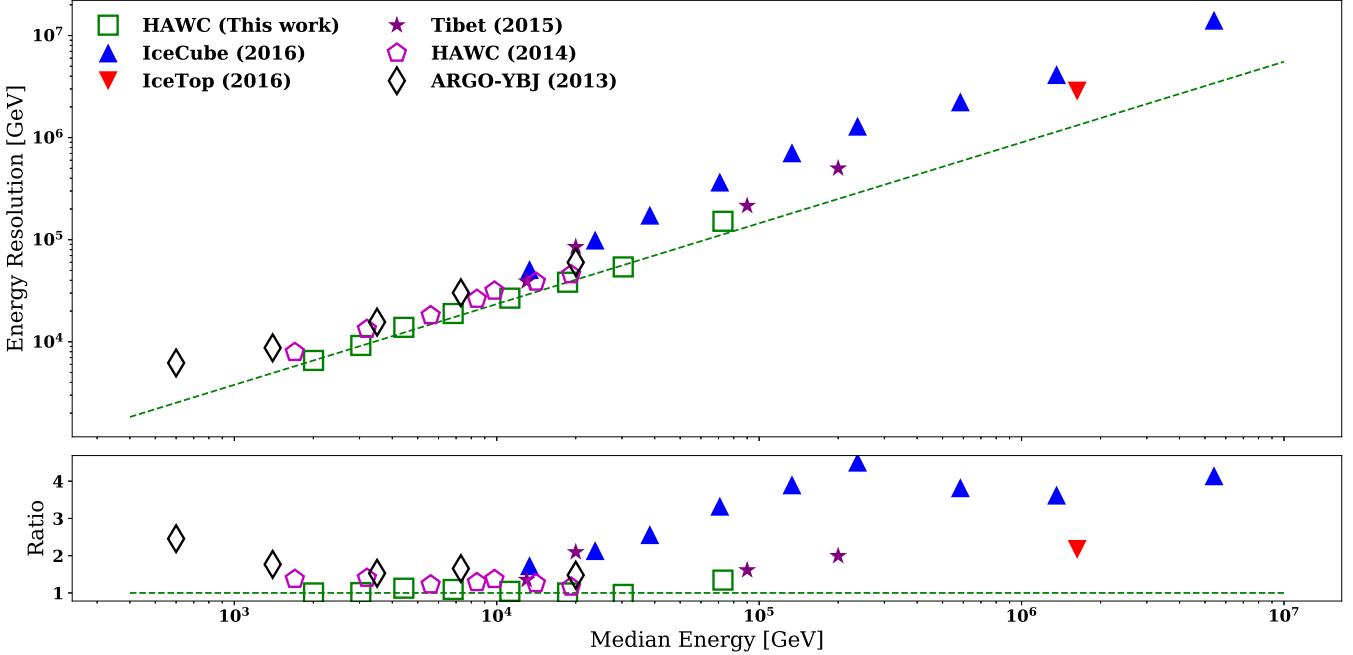
2. THE HAWC DETECTOR

The High-Altitude Water Cherenkov (HAWC) Gamma-Ray Observatory is an extensive air-shower array located at 4100 m a.s.l. on the slopes of Volcan Sierra Negra at 19°N in the state of Puebla, Mexico. While HAWC is designed to study the sky in gamma rays between 500 GeV and 100 TeV, it is also sensitive to showers from primary cosmic rays up to multi-PeV energies.

The detector consists of a 22,000 m^2 array of 300 close-packed water Cherenkov detectors (WCDs), each containing 200 kiloliters of purified water and four upward-facing photomultiplier tubes (PMTs). As secondary air shower particles pass through the WCDs, the Cherenkov light produced is collected by the PMTs, permitting the reconstruction of primary particle properties including the local arrival direction, core location, and the energy. Further details on the HAWC detector can be found in (Abeysekara et al. 2017).

The light-tight nature of the WCDs allows the detector to operate at nearly 100% up-time efficiency, with the data acquisition system recording air showers at a rate of ~ 25 kHz. With a resulting daily sky coverage of 8.4 sr, HAWC is an instrument well-suited for measuring the cosmic-ray arrival direction distribution.

3. THE DATA SET

The data set for this study consists of 508 uninterrupted sidereal days between 1 May, 2015 and 1 May, 2017. The detector operated with 294 WCDs, recording about 1.2×10^{12} air shower triggers. To determine the energy of the primary air shower particle, we apply a maximum likelihood-based estimator that uses the lateral distribution of measured PMT signals as a function of simulated primary proton energy (Alfaro et al. 2017). To improve the estimated energy resolution, poorly reconstructed showers are removed from the data set by application of moderate event selection. The selection criteria are:
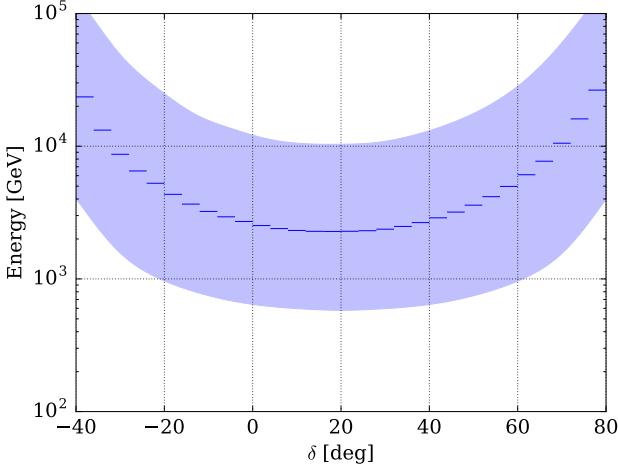
Figure 1. The energy resolution for previous cosmic-ray anisotropy measurements (using the multiplicity method) compared to the maximum-likelihood energy estimator used in this analysis. The improvement is about 30% below 10 TeV from previous HAWC results. A dashed green line connecting the first and sixth HAWC energy bins is shown to guide the eye. Ratios relative to that green line are shown in the lower panel. The energy resolution values for HAWC (Abeysekara et al. 2014) as well as IceCube and IceTop (Aartsen et al. 2016) are given in their publications. For ARGO-YBJ (Di Sciascio 2013) and Tibet (Amenomori et al. 2017), the values were estimated as the full-width at half-maximum of the provided energy distributions.

1. Air shower events must pass a minimum multiplicity threshold of ≥ 75 PMTs. This improves angle and energy reconstruction accuracy.

2. At least 1 PMT within 40 meters of the core position ($N_{\mathrm{r}40} \geq 1$) must record a signal. This criterion selects air showers landing on or near the array, resulting in a core resolution of better than 15 meters above 10 TeV.

3. The zenith angle acceptance range is $0° - 60°$.

4. The data set is composed of periods covering complete sidereal days, hence events from incomplete days are not included. This removes non-uniformities in sky exposure along right ascension, reducing systematics in the estimation of the reference map (see Section 4.1).

Requiring a multiplicity of ≥ 75 PMTs reduces the trigger rate to 23%. The remaining selection criteria further reduce the number of events by 52%, leaving a total of 123 billion air shower events.

Using the selection criteria and the likelihood energy estimator, we achieve $\sim 30\%$ improvement in energy resolution compared to the multiplicity energy-proxy method from previous HAWC results (Abeysekara et al. 2014), and a $\sim 50\%$ improvement over ARGO-YBJ (Di Sciascio 2013) below 10 TeV. This also permits more energy bins, as well as an increase in the median energy of the highest-energy bin. The median energy and 68% containment for the eight analysis bins are listed in Table 1 and

Figure 2. Median energy as a function of declination for the combination of all energy bins. The blue band indicates the 68% central containment region.

shown in Figure 1 along with the energy bins from comparable experimental results.

The estimated energy exhibits a slight dependence on declination as determined by simulation, shown in Figure 2. This is attributed to an increasing energy threshold with increasing zenith angle, as air showers must traverse more atmospheric overburden. The values presented in Figure 1 and Table 1 were calculated for the overhead sky ($\delta = 19°$), thus this declination-dependent energy shift must be considered when viewing the resulting sky maps.

Furthermore, for all maps in the lowest energy bin (2.0 TeV), there is a decreased range in declination used for analysis, corresponding to the first two zenith bins ($\theta < 35.2°$) of the energy estimation described in (Alfaro et al. 2017). This is due to the limited number of selected events having both large zenith angles and low reconstructed energies available to measure the anisotropy via the methods described in Section 4.

The estimated angular resolution given the selection criteria improves from $0.8°$ to $0.5°$ between 1 and 10 TeV, and plateaus at $0.5°$ above 10 TeV. A full description of the *in-situ* an-

gular resolution and energy-scale verifications with the cosmic-ray Moon shadow is presented in (Alfaro et al. 2017).
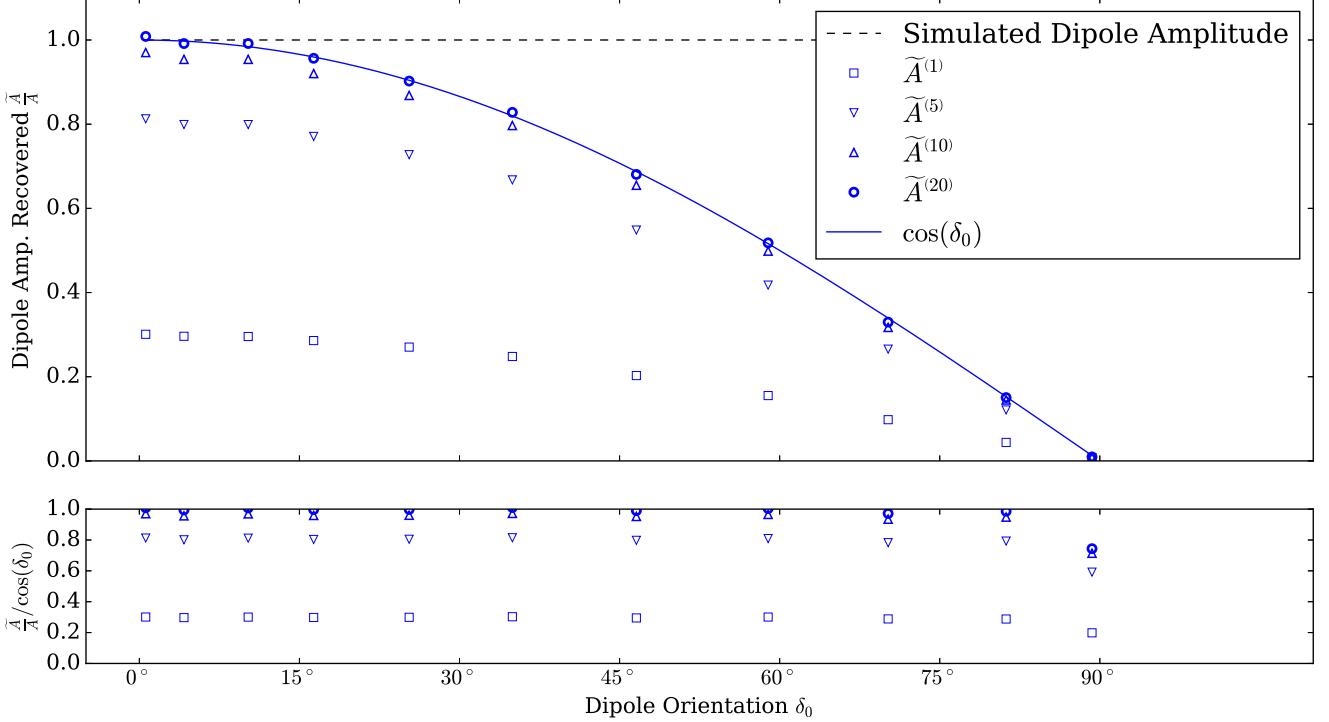
4. ANALYSIS

The measured anisotropy requires comparison of the observed data event distribution $\mathcal{D}$ with a background distribution or "reference map" $\mathcal{B}$, which represents the detector response to an isotropic flux of cosmic rays. This reference map is not in itself isotropic because of effects of the detector exposure and geometry. In principle, the reference map can be obtained from a complete simulation of the detector response to an isotropic flux of cosmic rays, but as previously mentioned, measuring anisotropy at the 10^{-4} level requires an accuracy of the detector simulation that can currently not be achieved for detectors like HAWC. The reference map is therefore estimated from the data themselves.

We report the anisotropy distribution using two-dimensional sky maps, represented via the equal-area pixellation scheme provided by the HEALPix (Gorski et al. 2005) package. Maps are tessellated with 12 base pixels, and each pixel is further partitioned into N_{side} subdivisions. We chose a fine pixellation of $N_{side} = 256$, corresponding to a pixel width of $0.23°$ and solid angle of 1.6×10^{-5} sr.

4.1. *Reference Map (Isotropic Expectation)*

The reference map is determined using the method described in (Atkins et al. 2003), due to its minimal assumptions on the data compared to similar background estimation methods (Amenomori et al. 2005b; Aglietta et al. 2009). This technique uses the number of events in local angular coordinates (the local detector acceptance) and in sidereal time (all-sky rate) to construct the expected counts map from an isotropic flux expectation.

For the calculation of the relative intensity of the cosmic-ray anisotropy, this paper uses for the first time a new analysis technique devel-

Figure 3. Fit to δI at 1, 5, 10, and 20 iterations (given by the superscript on $\tilde{A}$) for 10 simulated HAWC datasets with an injected dipole (oriented with δ_0 between $0°$ and $90°$) plus Poisson noise. This demonstrates the necessity of the convergence of iterative background estimation (light to dark blue points) in order to reach the maximally recoverable signal shown by the blue curve. For our method, the maximally recoverable signal is the projection of the dipole onto the right ascension axis. The black dashed line at $\frac{\tilde{A}}{A} = 1$ shows the relative true strength of the simulated dipole. For comparison, the amplitudes given by $\tilde{A}^{(1)}$ (squares) are equivalent to performing direct integration with $\Delta t = 24$hr (Ahlers et al. 2016).

oped by (Ahlers et al. 2016) which mitigates a common artifact of previous methods. For mid-latitude detectors like HAWC, methods like (Atkins et al. 2003) severely underestimate the relative intensity of any large-scale structure, in particular the strength of the dipole component. The reason for this underestimation is the fact that these detectors have an instantaneous field of view that is much smaller than the size of the large-scale anisotropy structure. As a consequence, these large-scale structures are attenuated.

Over the course of a sidereal day, as the Earth rotates, the detector eventually accumulates an event distribution that shows the entire large-scale structure. However, a consequence of observing different parts of the anisotropy at different times is that the observed event distribution is a function of both the instantaneous detector exposure as well as the cosmic-ray anisotropy itself.

The new method overcomes the effect of the limited instantaneous exposure by simultaneously fitting for the anisotropy and the detector exposure, using a maximum likelihood technique. The resulting equations cannot be solved explicitly, but best-fit solutions can be attained by iteratively adjusting the local acceptance and all-sky rate. The convergence criterion depends on the likelihood value of the calculated $\mathcal{B}$ provided $\mathcal{D}$ compared to the previous iteration.

Typically, the calculation requires less than 20 iterations.

We demonstrate the stable convergence of the process with simulated dipoles of various orientations on the sky using a set of 10^{10} simulated events drawn from a HAWC-like sky exposure. The rate as a function of sidereal time was varied by a simple sinusoid of amplitude 5%. On top of the simulated events, dipoles of strength 10^{-3} with ten different orientations in declination (δ_0, from 0–90 degrees) were added, providing ten fake data sets. For each simulated data set, the differential relative intensity map was created using the iterative method, and the maximally recoverable dipole amplitude was then obtained. Figure 3 shows the stable convergence of the fit results after 1, 5, 10, and 20 iterations. We also simulated various sky coverages confirming that the fit obtains the maximally recoverable dipole amplitude.

The all-sky rate varies by $\sim 5\%$ due to diurnal pressure cycles in the upper atmosphere, and the local detector acceptance is verified to be stable for each sidereal day by evaluating the χ^2-difference of local angular distributions in 2 minute intervals compared to the mean calculated over the entire sidereal day. With such minimal variations over the data set, we chose to sum the local detector acceptance and all-sky rate for all 508 sidereal days prior to the background calculation. Since the all-sky rate is binned in sidereal time bins of $1°$, much smaller than the large- and small-scale features ($> 10°$), variations within a single sidereal time bin have negligible impact on the observed features.

4.2. *Relative Intensity and Significance Map*

The amplitude of the measured anisotropy and its statistical strength are given by the sky maps in differential relative intensity δI and significance S, respectively. For a given pixel, δI is the fractional difference between the observed counts in that pixel, $\mathcal{D}$, and the expected counts from the reference map, $\mathcal{B}$:

$$\delta I = \frac{\mathcal{D}}{\mathcal{B}} - 1 \quad . \tag{1}$$

The significance of δI is conservatively estimated via

$$S \simeq \sqrt{\frac{\mathcal{D}}{1 + \alpha_{\mathrm{exp}}}} \delta I \quad , \tag{2}$$

based on (Li & Ma 1983), where α_{exp} is the relative exposure of the data map compared to the reference map. The reference map is overexposed compared to the data because it uses information from all local pixels to calculate its values. The value of α_{exp} is found analytically via the method in (Atkins et al. 2003), but a direct calculation was not determined for the iterative method. A conservative value of $\alpha_{\mathrm{exp}} = 1$ underestimates the statistical significance by at most 70%.
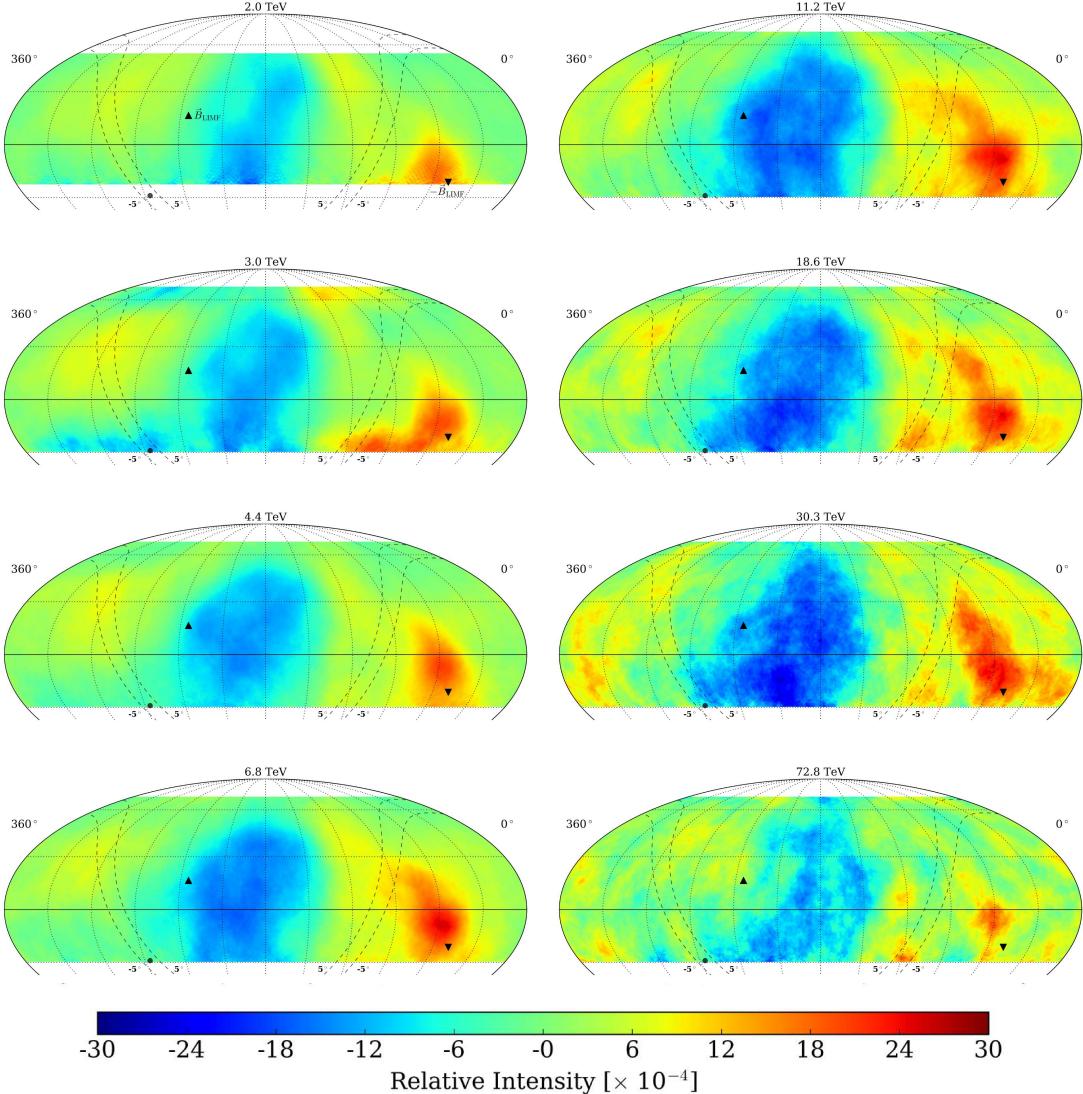
The results of the HAWC analysis are shown in Figure 4, which depicts the relative intensity of the arrival direction distribution of cosmic rays in equatorial coordinates for eight independent energy bins ranging from 2.0 to 72.8 TeV. Figure 5 shows the significance of the deviation from isotropy for the same energy bins, where negative values of significance correspond to pixels with $\delta I < 1$. The maps show significant deviation of the cosmic-ray flux from isotropy, dominated by a dipolar feature which increases in strength up to 30.3 TeV while maintaining a nearly constant phase.

4.3. *Multipole Fitting*

To better quantify the observed large-scale features, the relative intensity map δI is fit to the following truncated series of spherical harmonics:

$$\delta I = \sum_{\ell=1}^{\ell_{\mathrm{max}}} \sum_{m=-\ell}^{\ell} a_{\ell m} Y_{\ell m}(\theta, \phi) \quad (m \neq 0), \tag{3}$$
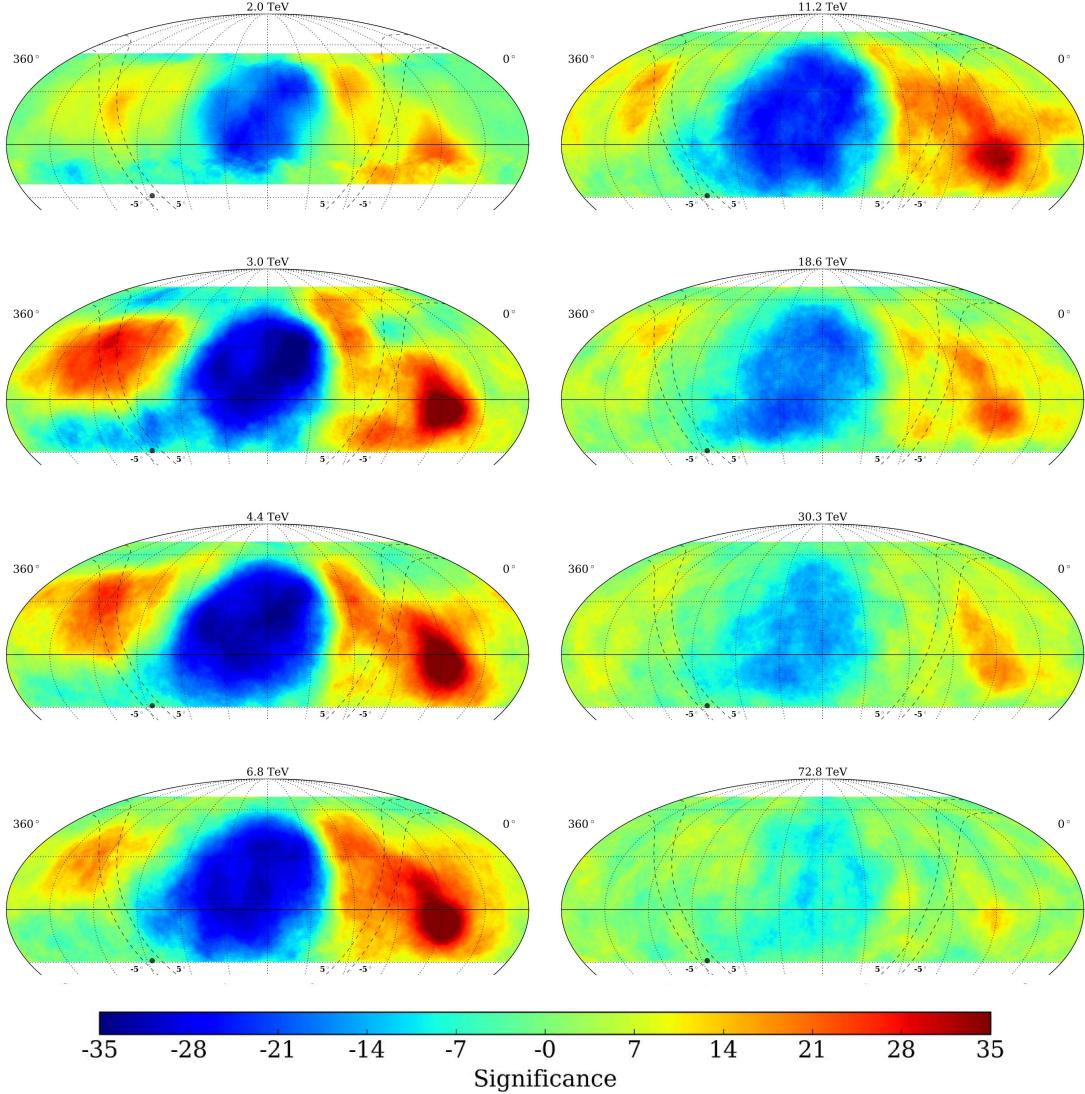
where ℓ_{max} is chosen to distinguish between large-scale and small-scale features. The choice of ℓ_{max} will be discussed in Section 5.

Figure 4. Anisotropy maps in differential relative intensity δI (smoothed $10°$) for eight energy bins separated by a likelihood-based reconstructed energy variable. Energies are reported as the median with the 68% containment of the bin according to simulation. The two triangle markers indicate the positive (upward-pointing) and negative (downward-pointing) directions of the local interstellar magnetic field $\vec{B}_{\mathrm{LIMF}}$ as inferred from Interstellar Boundary Explorer (IBEX) observations (Zirnstein et al. 2016). The Galactic Plane is shown with lines at $+5°$ and $-5°$ in Galactic latitude, and the Galactic Center is demarcated by the solid circle.

Since the local detector acceptance is estimated from the data, features in the anisotropy which only depend on declination can not be disentangled from declination-dependent asymmetries in the detector acceptance. This results from the fact that the HAWC detector only samples the sky in the Earth's rotational direction. Thus, we set $a_{\ell,0} = 0$ for all ℓ, i.e. the $m = 0$ terms, to reflect the knowledge that the analysis method is insensitive to anisotropy oriented solely along the declination direction.

Figure 5. Anisotropy maps in statistical significance (smoothed $10°$) for eight energy bins separated by a likelihood-based reconstructed energy variable.

In the fit, we chose to use the real-valued (tesseral) spherical harmonics,

$$Y_{\ell m}(\theta,\phi) = \begin{cases} \sqrt{\frac{2(2\ell+1)}{4\pi}\frac{(\ell-|m|)!}{(\ell+|m|)!}} P_\ell^{|m|}(x)\sin|m|\varphi & \text{if } m < 0 \\ \sqrt{\frac{2(2\ell+1)}{4\pi}\frac{(\ell-m)!}{(\ell+m)!}} P_\ell^m(x)\cos m\varphi & \text{if } m > 0 \end{cases}$$

(4)

where $x = \cos\theta$, again discarding the $m = 0$ terms which are symmetric in right ascension. The $a_{\ell m}$ are then determined by a χ^2-minimisation fit of δI to equation 3, and the variance for each pixel is calculated via propagation of uncertainties of the quantities $\mathcal{D}$ and $\mathcal{B}$ which comprise δI.

The strongest feature of the measured anisotropy is the dipole $(l = 1)$, which can be more conveniently expressed as an amplitude and phase by projection onto right ascension. The amplitude $\widetilde{A}_1$ can be expressed as the sum of the $a_{1,m}$ terms added in quadrature:

$$\widetilde{A}_1 = \sqrt{\frac{3}{8\pi}\sum_{m=1,-1}|a_{1m}|^2}$$

(5)

with variance

$$\sigma^2_{(\widetilde{A}_1)} = \frac{3}{8\pi \sum\limits_{m=1,-1} |a_{1m}|^2} \sum_{m=1,-1} \left(|a_{1m}|^2 \sigma^2_{(a_{1m})}\right). \quad (6)$$

The maximally recoverable dipole amplitude $\widetilde{A}_1$ obtained via the iterative method is related to the true amplitude A_1 through the original declination position of the maximum δ_0,

$$A_1 = \frac{\widetilde{A}_1}{\cos \delta_0}. \quad (7)$$

The term $a_{10} = 0$ leaves one term which scales with the cosine $(a_{1,1})$ and one that scales with the sine $(a_{1,-1})$ of the dipole phase $\widetilde{\phi}_1$. This constrains the maximum amplitude to a declination of $0°$, simplifying the measured phase to

$$\widetilde{\phi}_1 = \tan^{-1}\left(\frac{a_{1,-1}}{a_{1,1}}\right), \quad (8)$$

with variance

$$\sigma^2_{(\widetilde{\phi}_1)} = \frac{1}{\left(\sum\limits_{m=1,-1} |a_{1m}|^2\right)^2} \sum_{m=1,-1} \left(|a_{1m}|^2 \sigma^2_{(a_{1m})}\right). \quad (9)$$

4.4. Angular Power Spectrum

The cosmic-ray anisotropy is not a pure dipole, and its full angular power spectrum reveals the strength of correlations at various angular scales. Figure 6 shows for each energy bin the pseudo-angular power spectra as derived from the anafast routine in HEALPix, where $\tilde{C}_\ell = \frac{1}{2\ell + 1} \sum\limits_{m=-\ell}^{\ell} |a_{\ell m}|^2$. The infinite series of multipoles was truncated at $\ell_{\max} = 40$ for quicker computation. Truncation at the maximum multipole that can be calculated for a HEALPix grid ($\ell_{\max} = 3\,N_{\mathrm{side}} - 1$) was done for comparison, with no noticeable effect on the reported power spectra.

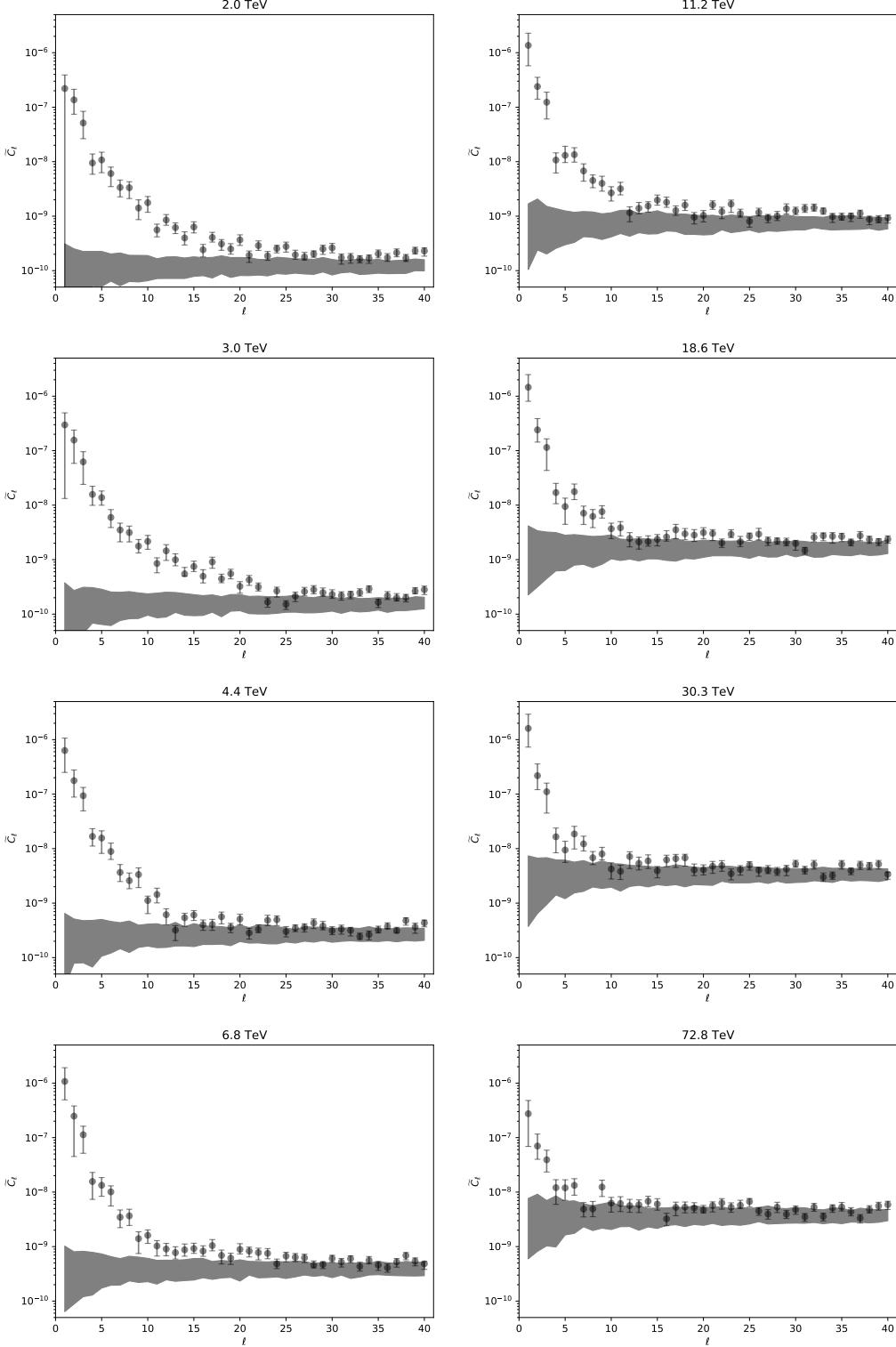The uncertainties shown in Figure 6 are systematic, representing the 68% central containment region of the measured power spectrum for maps generated to have the same power spectrum as the data. The statistical uncertainties are smaller than the data points. These were determined by the 68% containment of angular power spectra derived from random sky maps drawn from a Poisson distribution using the true map as the mean.

The gray band shows the 90% confidence interval for the expected angular power spectrum for an isotropic map containing the same event statistics. The isotropic power band is flat across the multipole moments, and its magnitude level is determined by the number of events in the map. This band was derived in the same way as the statistical uncertainties, except the data fluctuated by a Poisson distribution was compared to the true data instead of the reference map. The deviation of the spectral points from this gray band represents the measured signal strength compared to isotropy.
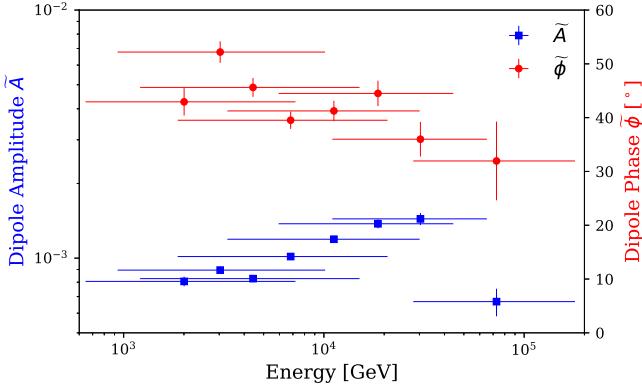
4.5. Systematics

As previously described, the measured dipole orientation in declination is unconstrained due to the limitations in estimating the reference map. For example, the measured amplitude (blue solid line in Figure 3) of a dipole with orientation $\delta_0 > 65°$ is decreased by more than a factor of two from its true value (black dashed line). By modeling the detector acceptance with functional forms, it is possible to recover the declination orientation as done in (Aab et al. 2017b). This systematic has not been studied for HAWC in this capacity, as it requires an inordinate amount of simulation that matches the data to a precision below the observed level of anisotropy. However, the degeneracies in the angular power spectrum caused by the lack of full sky coverage are taken into account in the systematic uncertaintes presented in Figure 6.

The known solar dipole signal from the motion of the Earth around the Sun is present in the data, and can in principle contaminate the dipole signal in equatorial coordinates. How-

Figure 6. Angular power spectra for each of the eight independent energy bins. The gray bands represent the power spectra for isotropic sky maps at the 90% confidence level. The uncertainties on the data points are systematic, representing the 68% containment of the measured angular power spectrum for maps with the same true power spectrum as the data. The statistical uncertainties are smaller than the data points. The multipole moments ℓ correspond to angular scales $180°/\ell$.

Figure 7. The best fit dipole amplitude (blue squares) and phase (red circles) as functions of energy.

ever, in this analysis, where an integer number of years of data taken at a constant rate is used, the influence of the solar dipole cancels and can be neglected. We estimate a maximum residual signal of 2×10^{-5} from the solar dipole, $\sim 1\%$ of the sidereal signal.

A thorough verification of the absolute energy scale has been performed using the energy dependence of the cosmic-ray Moon shadow (Alfaro et al. 2017). The uncertainty in the scale of the reported median energies for the eight analysis bins is estimated to be $\sim 5\%$.

5. RESULTS AND DISCUSSION

The resulting relative intensity maps, significance maps, and power spectra for each of the eight energy bins from 2.0 TeV to 72.8 TeV are shown in Figures 4, 5, and 6, respectively. The fit dipole amplitudes and phases obtained from these large-scale maps are shown in Figure 7. In order to enhance regional correlations, the sky maps have been smoothed by a circular top hat function of radius $10°$, in accordance with other studies (Abdo et al. 2008; Abeysekara et al. 2014).

Each map in Figure 4 shares the common significant features of having a broad region of deficit around $\alpha = 150°$ to $\alpha = 240°$ and a broad but more sharply-peaked excess around $\alpha = 30°$ to $\alpha = 90°$. The deficit grows in in-

tensity with energy until the final bin at 72.8 TeV, where the feature diminishes. The center of the excess starts low in the HAWC field of view near $\delta = -15°$ and rises to about $\delta = -5°$ by 4.4 TeV, where it remains for the remaining energy bins. Its strength increases until 11.2 TeV, slowly diminishing until nearly disappearing in the 72.8 TeV bin. Starting at 6.8 TeV the excess develops an extension higher in declination and slightly higher in right ascension. This extension is strongest in the 30.3 TeV bin before also diminishing by 72.8 TeV.

As shown in Figure 6, the dipole moments possess the most angular power for each bin, also reflected in the evolution of the broad deficit. The second strongest moment is the quadropole, whose power remains fairly constant at around 1.5×10^{-7} for all energies save the highest energy bin. The octupole moment is typically half of the quadrupole moment. In most bins there is a rapid decrease in power from these first three moments to the sextupole ($\ell = 4$), at which point we differentiate between the large and small angular scales. Significant anisotropy is seen up to $\ell = 10$ (characteristic angular scale of $18°$) until statistics dip below 5 billion events above 18.6 TeV.

The decrease in $\tilde{C}_\ell$ as a function of ℓ, especially for $\ell > 3$ becomes more rapid with increasing energy, and the anisotropy becomes less significant due to the rising noise floor of maps with fewer data. This noise level is represented as the expected power spectrum of an isotropic cosmic-ray distribution, shown by the gray bands in Figure 6. The large uncertainty for the $\ell = 1$ term in the lowest energy bin results from the reduced declination range available for the multipole fit. As the integrated sky coverage decreases, angular power from lower multipoles becomes increasingly degenerate with power from higher multipoles.

A summary of the dipole fit parameters obtained per the methods of Section 4.3, and

Table 1. Reported median energy (with 68% central containment region) and fit of two-dimensional dipole anisotropy (amplitude and phase) for each independent energy bin.

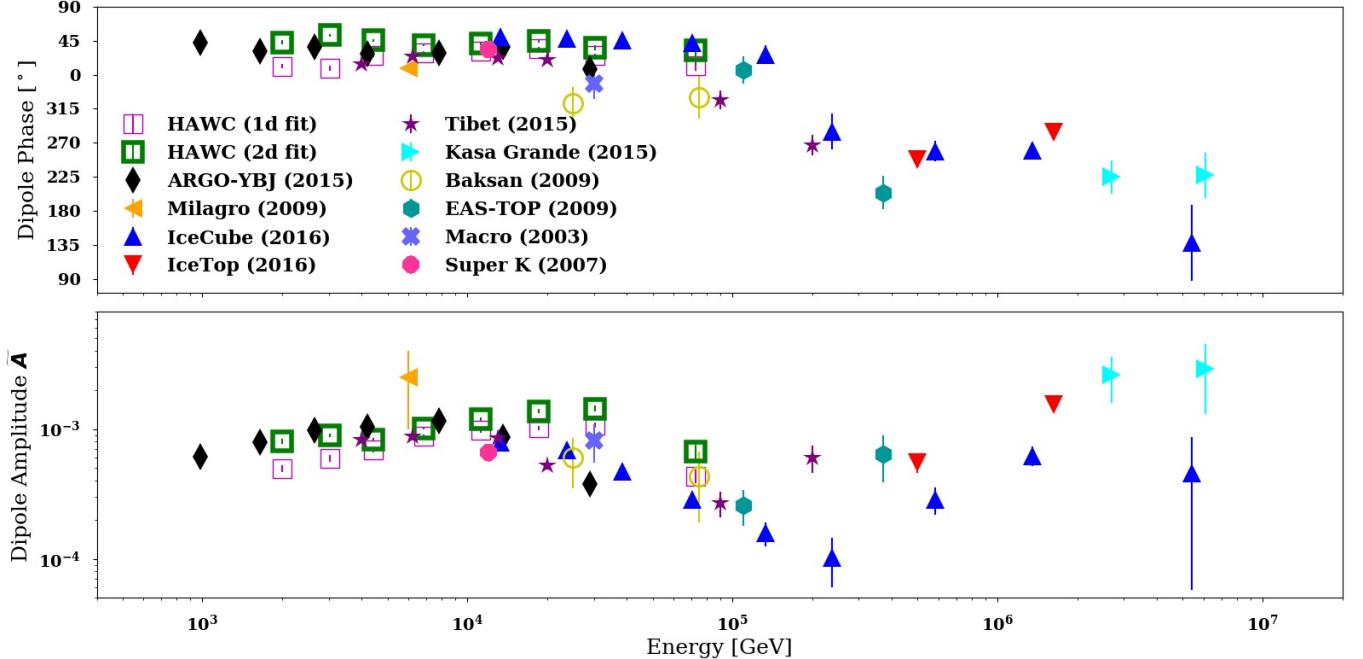| Energy [TeV]	Events	Amplitude $[\times 10^{-4}]$	Phase	$a_{1,1}$ $[\times 10^{-4}]$	$a_{1,-1}$ $[\times 10^{-4}]$	$\chi^2/N_{\rm dof}$
$2.0\left(^{-1.4}_{+5.2}\right)$	4.0×10^{10}	8.1 ± 0.4	$42.9° \pm 2.5°$	-17.1 ± 1.0	-15.9 ± 1.0	13.34
$3.0\left(^{-2.1}_{+7.1}\right)$	2.9×10^{10}	8.9 ± 0.3	$52.2° \pm 2.0°$	-15.9 ± 0.9	-20.5 ± 0.9	1.24
$4.4\left(^{-3.2}_{+10.6}\right)$	2.4×10^{10}	8.3 ± 0.3	$45.6° \pm 1.8°$	-16.7 ± 0.7	-17.1 ± 0.7	0.79
$6.8\left(^{-5.0}_{+14.0}\right)$	1.6×10^{10}	10.1 ± 0.3	$39.5° \pm 1.6°$	-22.7 ± 0.8	-18.7 ± 0.8	0.85
$11.2\left(^{-7.9}_{+18.8}\right)$	7.9×10^{9}	11.9 ± 0.4	$41.3° \pm 1.9°$	-25.9 ± 1.1	-22.7 ± 1.1	0.81
$18.6\left(^{-12.7}_{+25.6}\right)$	3.8×10^{9}	13.8 ± 0.6	$44.5° \pm 2.4°$	-28.4 ± 1.6	-27.9 ± 1.6	1.07
$30.3\left(^{-19.3}_{+34.8}\right)$	1.8×10^{9}	14.4 ± 0.8	$36.0° \pm 3.2°$	-33.7 ± 2.3	-24.5 ± 2.3	1.25
$72.8\left(^{-44.9}_{+106.7}\right)$	1.6×10^{9}	6.7 ± 0.9	$31.9° \pm 7.3°$	-16.4 ± 2.5	-10.2 ± 2.5	1.03

the median cosmic ray energies and numbers of events for each bin are given in Table 1. The dipole component is detected at a significant level in all bins, and as shown in Figure 7, its amplitude steadily increases with energy from 8.1×10^{-4} to 14.4×10^{-4} until the final bin at 72.8 TeV where its value drops to 6.7×10^{-4}. As shown in Figure 5, this bin also has the most significant excess near $\alpha = 300°$, the declination of the Cygnus region which has more than one extended TeV gamma-ray emission features. Determining the precise contribution of gamma-ray contamination will be considered in future studies.

The resulting phases and amplitudes from the dipole fits are compared with measurements from other experiments in Figure 8, with the HAWC measurements (green squares) being in fair agreement with the observed trends. Though not all phases are consistent within statistical errors, systematics which are not accounted for in the estimation of the reference maps may contribute to the $5° - 10°$ differences between HAWC and ARGO-YBJ (black diamonds) at energies below 10 TeV. The phases

measured by HAWC and IceCube are consistent within the overlapping energy range, noting that the reference map methods used here and in the IceCube study are nearly identical.

The evolution with energy of the fit amplitudes matches well with previous results, showing a steady rise until a sudden decrease between $50 - 100$ TeV. For the HAWC measurement, the highest energy bin at 72.8 TeV has nearly the same number of events as at 30.3 TeV, yet its dipole amplitude is reduced by more than half. The energy scale of the amplitude behavior is in slight disagreement with several other experiments. This tension could be resolved by shifting along the abscissa, as the experiments's energy scales may be offset relative to one another. For example, the energy scale reported for HAWC in this work may vary by 5% (Alfaro et al. 2017), while the ARGO-YBJ proton energy is reported to within 13% (Bartoli et al. 2015).

IceCube also shows a slight discrepancy in the amplitude scale of the anisotropy with other measurements, including HAWC. It is possible that differences in chemical compositions at de-
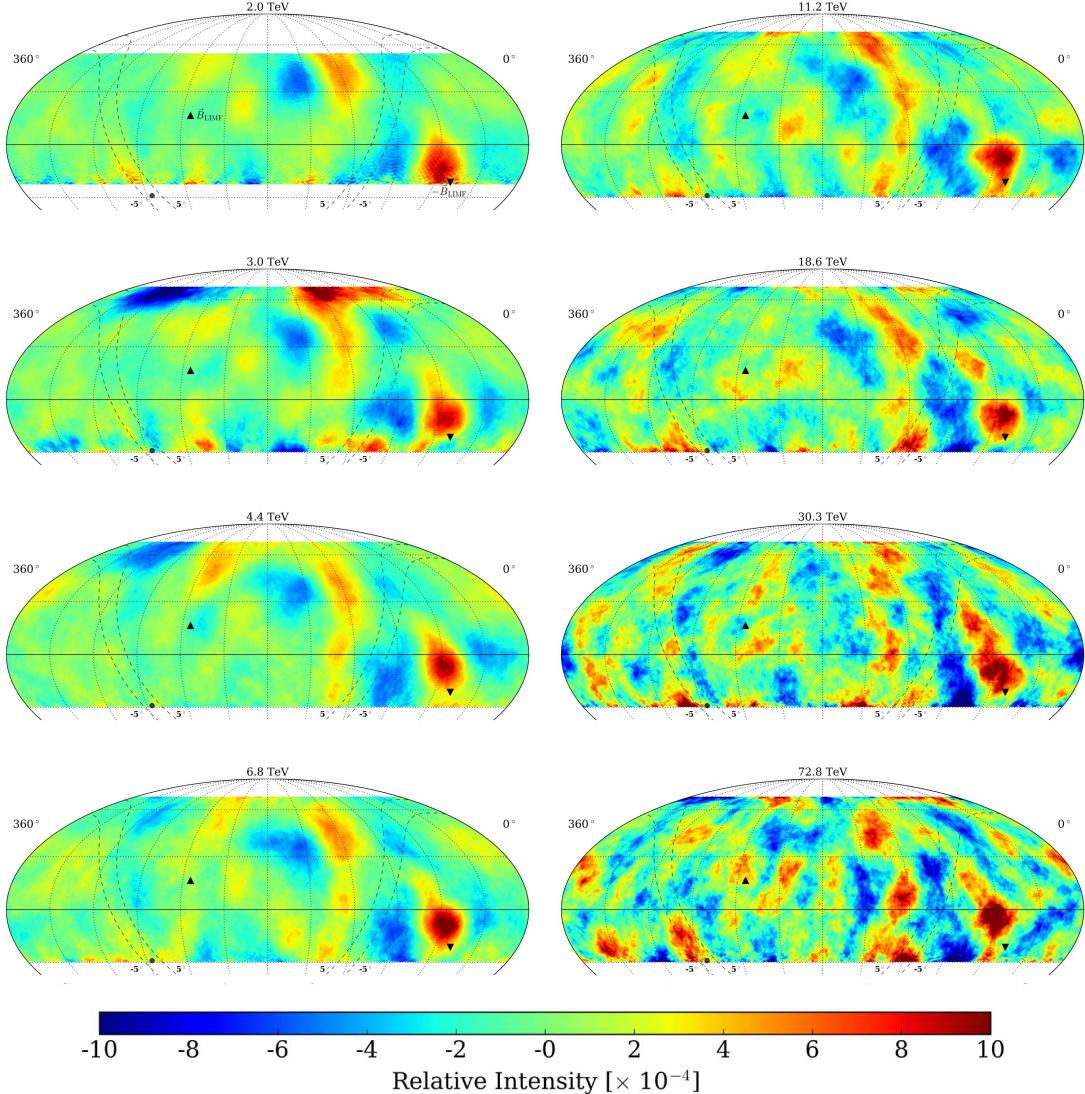
Figure 8. Comparison of the fit dipole phase (top) and amplitude (bottom) of HAWC and previously reported results for all-sky cosmic-ray anisotropy maps. All previous measurements fit the dipole projected in the right-ascension axis. The median energy for the energy bin is reported. The HAWC data is shown for both the method described in the paper (2d fit) and using the projection method (1d fit). The most notable feature across energies is the abrupt decrease in amplitude around 100 TeV. Above 100 TeV, the dipole reappears with a similar amplitude, but the phase has changed by nearly 180° (Aartsen et al. 2016; Amenomori et al. 2017).

tector level are the cause, as according to simulations IceCube measures a higher-rigidity composition than IceTop (Aartsen et al. 2016) and potentially other ground-based air shower detectors. While higher-rigidity particles follow field lines more closely, an anisotropy signal from many parsecs away might be distorted and diminished by the nearby magnetic fields of the Earth and the Sun. For reference, using the simulated composition described in (Alfaro et al. 2017), we find that the fraction of events passing the selection criteria from proton and helium primaries decreases with energy from 91% at 3 TeV to 78% at 10 TeV, and to 69% at 100 TeV.

In Figure 8 only the HAWC measurement shown by the green squares uses a two-dimensional fit as described in Section 4.3. All previous measurements represent fits of the dipole component to a Fourier series after projection of

the relative intensity sky map onto a single declination band. To match the method presented by the other experimental results, we also include one-dimensional fit dipole parameters (purple squares), being between 75–85% of the two-dimensional fit values. This suggests that previous dipole amplitudes also are underestimated, primarily affecting results from detectors with larger integrated fields-of-view (*e.g.* HAWC, ARGO-YBJ, and Tibet) as compared to those with more limited fields-of-view such as IceCube.
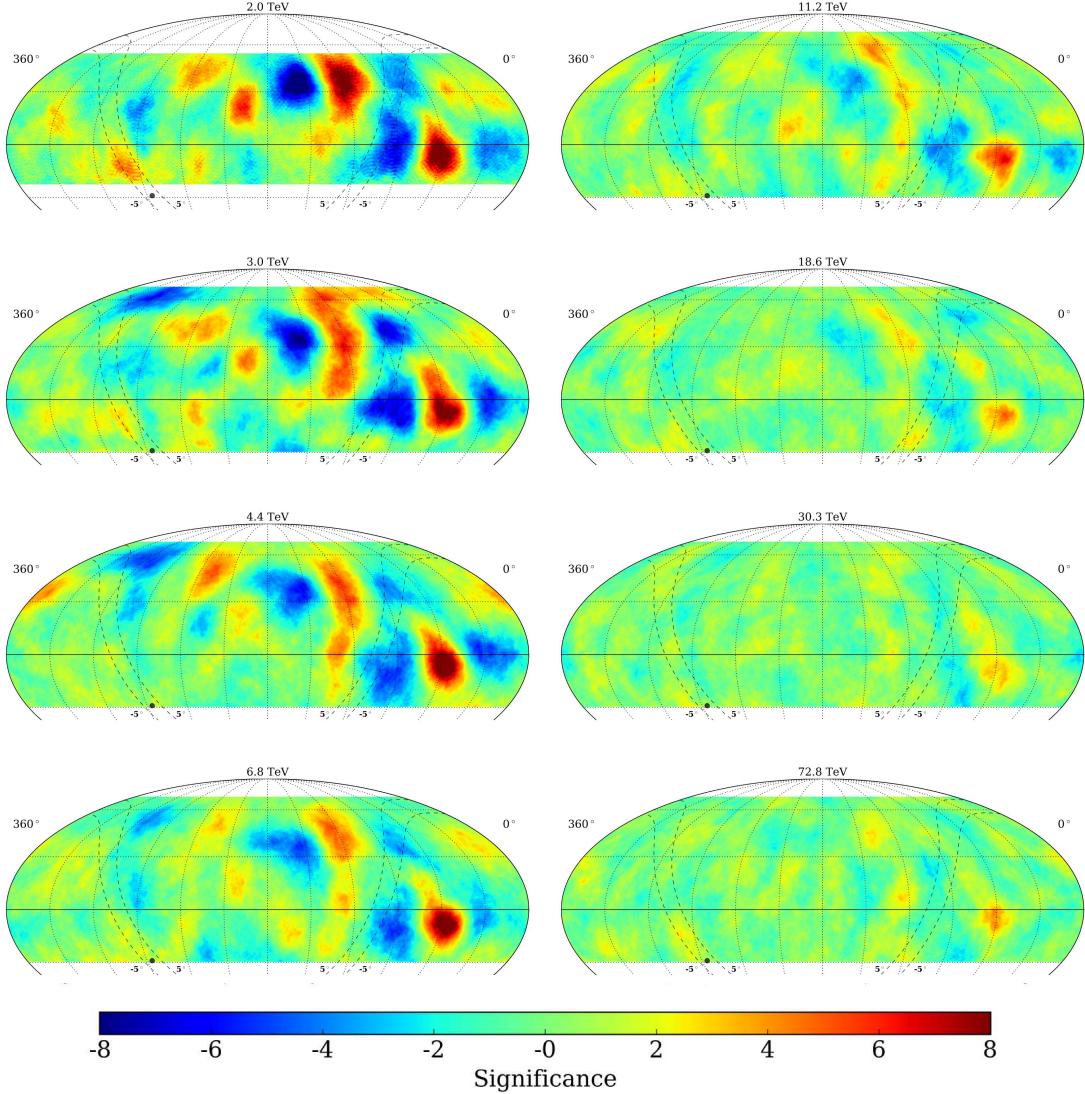
In addition to the large-scale structure, the sky maps have significant angular power at small angular scales ($\ell \geq 4$) as shown in the angular power spectra, and in the relative intensity and significance maps after subtraction of the $\ell \leq 3$ fit multipoles, shown in Figures 9 and 10. The three most significant regions of

Figure 9. Small-scale anisotropy maps in differential relative intensity δI (smoothed $10°$) for eight energy bins separated by a likelihood-based reconstructed energy variable. A multipole fit to the moments with $\ell \leq 3$ has been removed. The two triangle markers indicate the positive (upward-pointing) and negative (downward-pointing) directions of the local interstellar magnetic field $\vec{B}_{\mathrm{LIMF}}$ as inferred from Interstellar Boundary Explorer (IBEX) observations (Zirnstein et al. 2016). The Galactic Plane is shown with lines at $+5°$ and $-5°$ in Galactic latitude, and the Galactic Center is demarcated by the solid circle.

excess previously observed with Milagro (Abdo et al. 2008) and HAWC (Abeysekara et al. 2014) are Regions A, B, and C (referred to as Regions 1, 2, and 4 by ARGO-YBJ (Bartoli et al. 2013)). These are more apparent in the relative intensity and significance maps of Figure 11, where all events have been combined into a single map having median energy of 2.6 $\left(^{-2.0}_{+9.9}\right)$ TeV

to study each region's morphology. The excess defined as Region 3 by ARGO-YBJ (Bartoli et al. 2013) has a maximum significance of $4.6 \ \sigma$ at $\alpha = 251.2°$, $\delta = 19.5°$ in the combined HAWC map, with a mean relative intensity for the entire region of $(1.4 \pm 0.3) \times 10^{-4}$, approximately 14% greater than that measured by
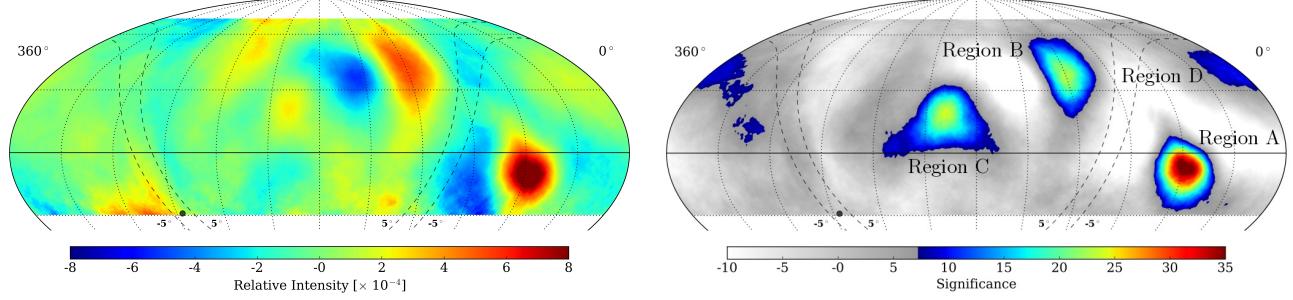
Figure 10. Small-scale anisotropy maps in statistical significance (smoothed 10°) for eight energy bins separated by a likelihood-based reconstructed energy variable. A multipole fit to the moments with $\ell \leq 3$ has been removed.

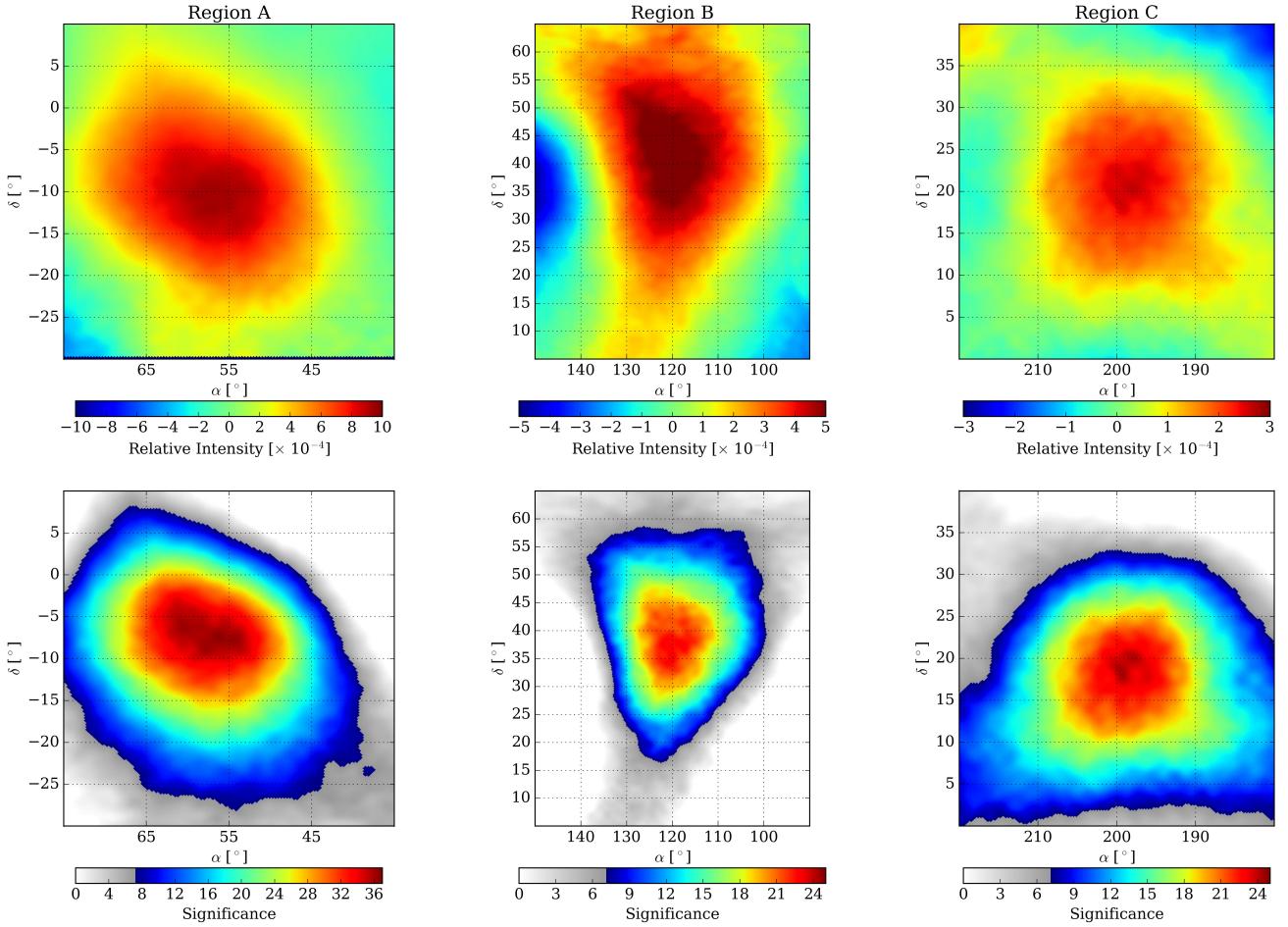ARGO-YBJ. Figure 12 shows zoomed-in views of each regional excess observed by HAWC.

Regions A and C are characterized as relatively symmetric excesses with extent of $\approx 30°$, as compared to Region B, which has a similar width in right ascension but is elongated by nearly a factor of two in declination. Similar morphology was observed for all three regions in the previous small-scale study by HAWC (Abeysekara et al. 2014). A significant feature previously not observed by HAWC nor ARGO-

YBJ is labelled Region D in Figure 11. This new excess occupies about 25° in declination while also being elongated by about a factor of two in right ascension, though is considerably weaker than the other regions, having a maximum relative intensity of $(1.7 \pm 0.2) \times 10^{-4}$.

Region A is the most prominent feature in δI as seen in Figure 9, being present at all energies, while the shape of Region B is evident up to 18.6 TeV and that of Regions C and D are difficult to discern given the color scale. The
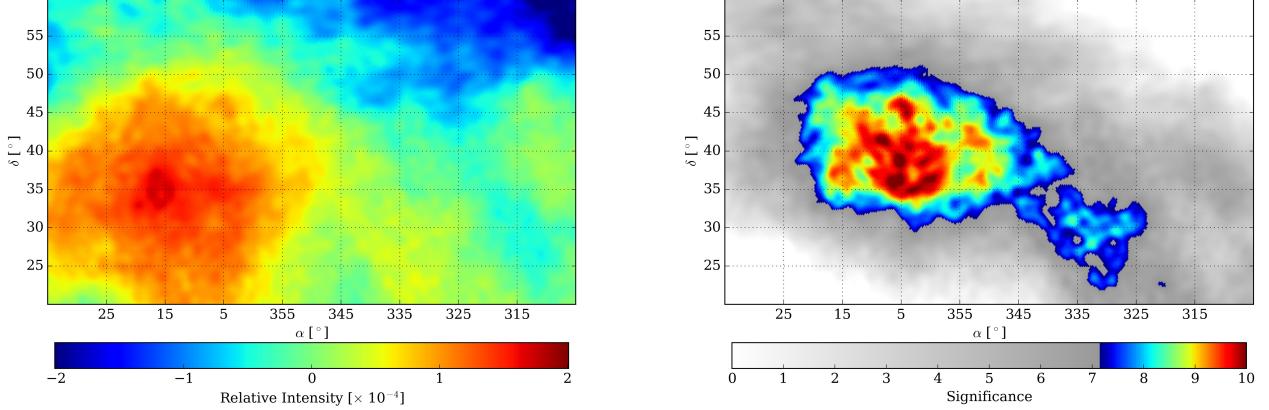
Figure 11. Relative intensity (left) and significance (right) maps for all analysis bins combined, showing the locations of the most significant excesses, Regions A, B, C, and the new Region D. The estimated median energy of the combined map is $2.6 \left({}^{-2.0}_{+9.9} \right)$ TeV, where the limits represent 68% containment.

Figure 12. Localized views of the relative intensity (top row) and significance (bottom row) of Regions A (left), B (center), and C (right) having combined all energy bins into a single map. The coordinates of the maximally significant pixels found for each region are presented in Table 2. The scales for the relative intensity and significance are different for each region.

presence of these features in significance as a function of energy is shown in Figure 10, with

Figure 13. Localized views of the relative intensity (left) and significance (right) of Region D having combined all energy bins into a single map. The coordinates of the most significant pixel is presented in Table 2.

Regions A and B being significant up to 18.6 TeV, Region D peaking at 4.4 TeV and Region C being strongest below 4.4 TeV.
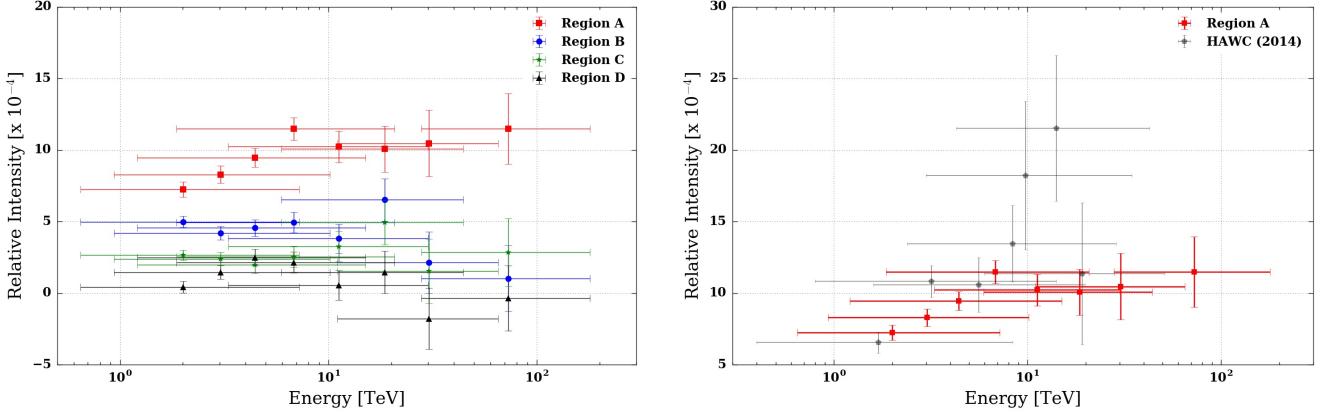
Table 2 presents for the four regions the locations in (α, δ) of the peak significances ($\sigma_{\max}$) and the corresponding δI values found in the all-bins combined maps. The relative intensity values are consistent with those found for Regions A, B and C at $\sigma_{\max}$ in (Abeysekara et al. 2014), while the locations of $\sigma_{\max}$ are shifted by $\sim 5°$ from their previously identified values. The relative intensity spectra as a function of energy extracted from the maps in Figure 9 at these locations are shown in Figure 14, including that of Region D. Regions B and C are characterized by relatively flat spectra across the energy bins as compared to that of Region D, which increases in δI up to the 4.4 TeV bin before decreasing, and Region A which has a positive slope up to 6.8 TeV. This is consistent with the previous spectral measurement of Region A by HAWC (Abeysekara et al. 2014) as shown in the right panel of Figure 14. Due to improved uncertainties from a data set an order of magnitude greater, the shape of the spectrum from this study is much more constrained, especially for $E \geq 10$ TeV. As was done in (Abeysekara et al. 2014), we estimate the statistical significance of the spectral slope of Region A by com-

paring a linear fit of $\delta I(\log E)$ to similar fits performed across the field of view. The distribution of slopes across the sky (excluding points within $20°$ of Regions A, B, C, and D) follows a Gaussian distribution with mean of zero and width 0.69×10^{-4}. The slope fit at the location of Region A is $(1.66 \pm 0.46) \times 10^{-4}$, falling $2.4\,\sigma$ from the all-sky mean.

From Figures 4 and 9 it appears that the large-scale structure as well as Region A are approximately oriented along the local interstellar magnetic field $\vec{B}_{\mathrm{LIMF}}$ inferred from Interstellar Boundary Explorer (IBEX) measurements. In equatorial coordinates (α, δ), this direction is $(234.43° \pm 0.69°, 16.3° \pm 0.45°)$, and $(48.5° \pm 0.69°, -21.2° \pm 0.45°)$ for $-\vec{B}_{\mathrm{LIMF}}$ (Zirnstein et al. 2016). This alignment is consistent with local conditions playing a role in shaping the observed cosmic-ray anisotropy, providing insight into the structure of the local interstellar medium and the heliospheric environment (Desiati & Lazarian 2013; Schwadron et al. 2014).

6. CONCLUSIONS

The HAWC Observatory has observed significant cosmic-ray anisotropy on both large and small scales using 123×10^9 events comprising one of the largest TeV anisotropy data

Figure 14. Left: relative intensity spectra as a function of energy for Regions A, B, C, and D. Right: comparison of the relative intensity spectra for Region A from this study and the previous HAWC measurement (Abeysekara et al. 2014).

Table 2. Locations and relative intensities of maximal significance found in the combined map for Regions A, B, C, and D.

Region	$\sigma_{\max}$	$\delta I\ [\times 10^{-4}]$	$\alpha\ [°]$	$\delta\ [°]$
A	36.6	9.0 ± 0.3	56.4	-7.5
B	23.0	5.3 ± 0.2	118.0	37.5
C	24.4	2.6 ± 0.2	199.3	18.1
D	10.3	1.3 ± 0.2	5.3	38.9

sets to date. Implementing an energy estimation technique that has been verified using the cosmic-ray Moon shadow (Alfaro et al. 2017), we have achieved an unprecendented energy resolution for measuring the energy-dependence of the anisotropy over eight analysis bins. Additionally, a new maximum-likelihood method was used to recover a minimally-biased estimate of the expected intensity of an isotropic signal.

The energy dependence of the large-scale phase and amplitude is found to be consistent with observations made by other detectors in the Northern Hemisphere. Similarly, the morphology and relative intensity spectra of the three most significant small-scale regions of excess are consistent with previous measurements made by HAWC (Abeysekara et al. 2014) and ARGO-YBJ (Di Sciascio 2013; Bartoli et al. 2013, 2015). Finally, due to the increased statistics of the current data set, it is possible to further constrain the spectrum of Region A from previous Milagro and HAWC measurements.

Along with continued optimization of the event selection, the ever-growing HAWC data set will facilitate increasingly accurate descriptions of the anisotropy as a function of energy, providing additional insights into the nature of local accelerators and the interstellar environment. Furthermore, the novel techniques used in this study allow for collaboration with other observatories using data sets consisting of targeted cosmic-ray energy bands. Combination of HAWC data with the IceCube cosmic-ray data set is an ongoing effort which will form a nearly complete map of the cosmic-ray sky at TeV energies.

REFERENCES

Aab, A., et al. 2017a, JCAP, 1706, 026

—. 2017b, Science, 357, 1266

Aartsen, M., et al. 2013, Astrophys.J., 765, 55

Aartsen, M. G., et al. 2016, Astrophys. J., 826, 220

Abbasi, R., et al. 2010, Astrophys. J., 718, L194

—. 2011, Astrophys.J., 740, 16

—. 2012, Astrophys.J., 746, 33

Abdo, A. A., et al. 2008, Phys. Rev. Lett., 101, 221101

—. 2009, Astrophys. J., 698, 2121

Abeysekara, A. U., et al. 2014, Astrophys. J., 796, 108

—. 2017, Astrophys. J., 843, 39

Aglietta, M., et al. 2009, Astrophys. J. Lett., 692, L130

Ahlers, M. 2014, Phys. Rev. Lett., 112, 021101

Ahlers, M., BenZvi, S. Y., Desiati, P., et al. 2016, Astrophys. J., 823, 10

Ahlers, M., & Mertsch, P. 2015, Astrophys. J., 815, L2

—. 2016, Prog. Part. Nucl. Phys., arXiv:1612.01873

Alfaro, R., et al. 2017, Phys. Rev. D, 96, 122001. https://link.aps.org/doi/10.1103/PhysRevD.96.122001

Amenomori, M., et al. 2005a, Astrophys. J., 626, L29

Amenomori, M., Ayabe, S., Chen, D., et al. 2005b, The Astrophysical Journal, 633, 1005. http://stacks.iop.org/0004-637X/633/i=2/a=1005

Amenomori, M., et al. 2006, Science, 314, 439

—. 2017, Astrophys. J., 836, 153

Atkins, R. W., et al. 2003, Astrophys.J., 595, 803

Bartoli, B., et al. 2013, Phys.Rev., D88, 082001

—. 2015, Astrophys. J., 809, 90

Blasi, P., & Amato, E. 2012, JCAP, 1201, 011

Compton, A. H., & Getting, I. A. 1935, Phys. Rev., 47, 817. http://link.aps.org/doi/10.1103/PhysRev.47.817

Desiati, P., & Lazarian, A. 2013, Astrophys.J., 762, 44

Di Sciascio, G. 2013, EPJ Web Conf., 52, 04004

Di Sciascio, G., & Iuppa, R. 2014, arXiv:1407.2144

Drury, L. 2013, in Proc. 33rd ICRC, Rio de Janeiro, Brazil

Erlykin, A. D., & Wolfendale, A. W. 2006, Astropart. Phys., 25, 183

Giacinti, G., & Kirk, J. G. 2017, Astrophys. J., 835, 258

Giacinti, G., & Sigl, G. 2012, Phys.Rev.Lett., 109, 071101

Gorski, K., Hivon, E., Banday, A., et al. 2005, Astrophys.J., 622, 759

Harding, J. P., Fryer, C. L., & Mendel, S. 2016, Astrophys. J., 822, 102

Kumar, R., & Eichler, D. 2014, The Astrophysical Journal, 785, 129. http://stacks.iop.org/0004-637X/785/i=2/a=129

Li, T.-P., & Ma, Y.-Q. 1983, Astrophys.J., 272, 317

Mertsch, P., & Funk, S. 2015, Physical Review Letters, 114, 021101

Pohl, M., & Eichler, D. 2013, Astrophys. J., 766, 4

Schwadron, N., et al. 2014, Science, 343, 988

Sveshnikova, L. G., Strelnikova, O. N., & Ptuskin, V. S. 2013, Astropart. Phys., 50-52, 33

Zirnstein, E. J., et al. 2016, The Astrophysical Journal Letters, 818, L18. http://stacks.iop.org/2041-8205/818/i=1/a=L18